

Study of low-frequency quasi-periodic oscillations in GRS 1739–278 during 2014 outburst

Ilya A. Mereminskiy^{1*}, Andrey N. Semena¹, Alexander A. Lutovinov¹,
Sergey D. Bykov^{1,2}, Ekaterina V. Filippova¹

¹*Space Research Institute, Russian Academy of Sciences, Moscow, Russia*

²*Bauman Moscow State Technical University, Moscow, Russia*

Accepted XXX. Received YYY; in original form ZZZ

ABSTRACT

We detected a type-C LF QPO at 0.3–0.7 Hz in *NuSTAR* and *Swift-XRT* observations of the black hole candidate GRS 1739–278 during the hard-intermediate state of its 2014 outburst, and type-B QPO in 1.7–5.2 Hz range during the soft-intermediate state. We traced the evolution of spectro-timing properties of the source during *NuSTAR* observation. As QPO frequency increases, the source spectrum becomes softer, with increasing power-law index and decreasing cut-off energy.

We performed an extended analysis of rapid X-ray variability in terms of power spectrum, cospectrum, coherence and phase-lags. In the power spectrum a prominent QPO and its second harmonic are clearly seen. The fluxes in soft and hard X-ray bands are coherent, however coherence drops with the separation of the energy bands. Phase-lags are generally positive (hard) in the 0.1–3 Hz frequency range, and negative below 0.1 Hz. Measurements of the inner disk radius obtained with the spectral models accounting for the metric around black hole and QPO frequency together with the relativistic precession model points towards very massive black hole.

Key words: X-rays: individual (GRS 1739–278) – X-rays: binaries – accretion, accretion disks – stars: black holes

1 INTRODUCTION

A study of X-ray variability in accreting astrophysical sources provides a broad view on processes that take a place in such systems. This works both on a long timescales - i.e. days and weeks - when one speaks about state changes through outbursts of transients sources (see e.g. [Homan and Belloni 2005](#); [Heil et al. 2015](#)), and on short - all the way down to milliseconds - when the subject under consideration are a quasi-periodic oscillations (QPOs) and broad band stochastic noise. By simultaneous usage of spectral and timing data one can better constrain geometry of accretion flow around compact objects and infer on which processes are responsible for generation of observed spectro-timing features in a self-consistent way.

Some aspects of the spectro-timing evolution of X-ray transients (usually black-hole candidates, BHC) during outbursts can be explained in the frame of the two-temperature accretion flow model ([Eardley et al. 1975](#); [Shapiro et al. 1976](#); [Narayan and Yi 1995](#)), in which it is proposed that the accretion flow in a system consists of the geometrically

thin cold disk and geometrically thick hot flow (corona). It is strongly suggested from the observations that this geometrically thick hot flow is responsible for production of strong variability. As an example, using frequency-resolved spectroscopy [Churazov et al. \(2001\)](#) shown that variable part of the emission from the BHC system Cyg X-1 has a hard power-law shaped spectrum, which is thought to be produced by Comptonization of soft photons onto hot electrons in the corona, while stable part of the emission has a spectrum which is consistent with the cold classical α -disc spectrum ([Shakura and Sunyaev 1973](#)). It is also well known that total variability power of BHC and neutron star binaries is greater in the hard state (when the spectrum is dominated by the emission produced in the hot flow) than in the soft state (when the spectrum can be described with optically thick α -disc model) ([Miyamoto et al. 1992](#); [Revnivtsev et al. 2000](#); [Homan et al. 2001](#); [Churazov et al. 2001](#), e.t.c.). [Lyubarskii \(1997\)](#) proposed that observed strong variability (seen as a broad band noise in power spectra) is produced due to the stochastic variations of the angular momentum transport efficiency. In this propagating fluctuation model broad band noise of the luminosity is a product of noise signals from different radii of the accretion flow, each with its

* E-mail: i.a.mereminskiy@gmail.com

own characteristic time-scale (see, e.g. [Arévalo and Uttley 2006](#); [Ingram and van der Klis 2013](#)). Therefore, the spectral shape of the broad band noise is determined by the physical and geometrical properties of the accretion flow, e.g. in particular in these works it was suggested that the broad noise dumping frequency is connected to the inner edge of the accretion flow.

Another feature, frequently observed in the X-ray binaries power spectra is different types of low and high frequency QPOs, manifesting itself as a narrow Lorentzian components. The low frequency QPOs are better studied, since they occur at moderate frequencies of 0.1–10 Hz. This QPOs are ubiquitous - they found in systems with neutron stars and black holes ([Wijnands and van der Klis 1999](#)), in cataclysmic variables ([Mauche 2002](#)) and even in active galactic nuclei ([Gierliński et al. 2008](#)). Few types of LF QPOs are distinguished, based on the shape of power spectrum (see, e.g. [Casella et al. 2005](#)). Most importantly, their origin still remains unclear, although it is possible that different mechanisms are responsible for different types of QPO.

Type-C LF QPOs are typically found in X-ray black hole transients (yet they are known to be present in neutron star systems too) during initial rise and transition to disk dominated state - i.e. in low-hard state (LHS) and in hard intermediate state (HIMS), according to standard scheme ([Grebenev et al. 1997](#); [Tanaka and Shibazaki 1996](#); [Remillard and McClintock 2006](#); [Belloni 2010](#)), although they are sometimes seen at higher frequencies (≈ 30 Hz) after transition to high soft state (HSS). These QPOs are easy to detect and study, since they are prominent, having $rms \approx 10\%$ ([Casella et al. 2005](#)). Different authors prescribe generation of these QPOs to various processes: Lense-Thirring precession of inner parts of the accretion disk ([Stella and Vietri 1998](#); [Ingram et al. 2009](#)), oscillations of a standing shock ([Molteni et al. 1996](#)) and accretion rate modulation caused by different phenomena ([Tagger and Pellat 1999](#); [Cabanac et al. 2010](#)) e.t.c. In some models, particularly in relativistic precession models (RPM), observed frequency is strongly dependent on the inner radius of the accretion disk, at which it transforms into geometrically thick optically thin hot flow.

Recent advances in simulations of the reflected emission ([Ross and Fabian 2005](#); [García et al. 2014](#)), arising due to the scattering and absorption of the hard photons in the cold accretion disk, led to the possibility to study geometry of the disk. For such a study to be made it is essential to obtain broadband X-ray spectrum with high energy resolution - reflected emission manifest itself by a presence of prominent, wide and asymmetric iron K_α fluorescent emission line at 6.4 keV and Compton-hump at 20–30 keV. Now, adding information from X-ray timing analysis one can, in principle, constrain the location of a component, responsible for the variability - which is though to be a corona or a jet base. This task presents a challenge, that can be solved only by a telescope that possesses both possibility to measure a broadband spectrum with good resolution and have a corresponding timing capabilities. *NuSTAR* ([Harrison et al. 2013](#)), launched in 2013, is the best available instrument for such studies. *XMM-Newton* and *NICER* can be used too, although their energy range reaching only up to ~ 12 keV limits their capability to measure hard tails and Compton-hump contribution. Nevertheless there are some great results

obtained with these instruments, e.g. measurement of the Fe K_α line profile variation with QPO phase by [Ingram et al. \(2016\)](#).

In this article we report on first detection of type-C QPOs in HIMS of Galactic black-hole candidate GRS 1739–278 and present a detailed study of properties of the X-ray variability, along with spectral evolution with *NuSTAR* and *Swift-XRT*.

2 GRS 1739–278

GRS 1739–278 is a typical X-ray nova, discovered during outburst in 1996 ([Paul et al. 1996](#)) by *SIGMA* ([Paul et al. 1991](#)) telescope onboard *GRANAT* space observatory. Using *ROSAT* observation [Greiner et al. \(1996\)](#) inferred distance of 6–8.5 kpc from the estimated absorption, indicating that the source may belong to Galactic bulge. It should be noted that [Greiner et al. \(1996\)](#) used X-ray halo size to assess obscuration column density, and mean extinction per parsec value from ([Allen 1973](#)) to estimate distance to the source. While his N_H estimation appears to be quite precise it is larger than the new measurements of the line of sight absorption in the Galaxy towards the source ([Dickey and Lockman 1990](#); [Kalberla et al. 2005](#); [Marshall et al. 2006](#); [Schultheis et al. 2014](#)). It follows that the source either has intrinsic obscuration or additional line of sight obscuration and the distance to the source can not be constrained from N_H . Nevertheless in this work we will assume that the distance to GRS 1739–278 is 8 kpc, given that the source is projected on to the Galactic Bulge.

Optical and radio emission were detected during the course of outburst ([Hjellming et al. 1996](#); [Marti et al. 1997](#)). [Borozdin et al. \(1998\)](#) found spectral evolution throughout the outburst to be consistent with canonical model - outburst starts from LHS, then soft emission, associated with the optically thick disk starts to dominate, heralding transition to high soft state. Eventually, they observed very high state and detected a QPO at 5 Hz using *RXTE* data ([Borozdin and Trudolyubov 2000](#); [Wijnands et al. 2001](#)).

After some 18 year slumber GRS 1739–278 demonstrated another big outburst, rise of which was detected by *Swift-BAT* ([Krimm et al. 2014](#)) along with *INTEGRAL* ([Filippova et al. 2014](#)). During this outburst extensive observing campaign by *Swift-XRT* were carried out, along with single long *NuSTAR* exposure. After this outburst the source remain active with repetitive mini-outbursts ([Mereminskiy et al. 2017](#); [Yan and Yu 2017](#)).

3 OBSERVATIONS AND DATA REDUCTION

In order to characterize the overall outburst profile we used data of *Swift-BAT transient monitor* ([Krimm et al. 2013](#)) in hard X-rays (15–50 keV) as well as (2–4 keV) lightcurve from *MAXI* ([Matsuoka et al. 2009](#)).

We used *NuSTAR* observation (ObsID: 80002018002) performed at March 26, 2014 (MJD 56742). We utilized `nuproducts` pipeline to extract photons from two-arcminute circular region, centered on the source and to produce lightcurves and spectra.

We also used public observations of *Swift-XRT* (target

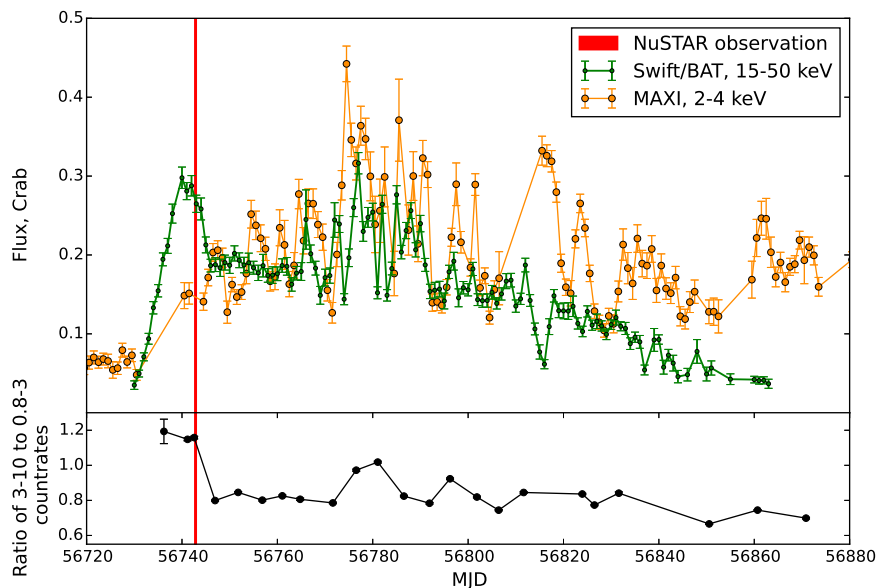


Figure 1. *Upper:* green points denote *Swift-BAT* lightcurve of 2014 outburst in 15–50 keV range, orange circles correspond to *MAXI* fluxes in 2–4 keV. Red line show the time interval of *NuSTAR* observation. *Lower:* evolution of *Swift-XRT* spectral hardness during the outburst.

ID: 33203) performed regularly over the rise and peak of the outburst. Since the source was bright, all *Swift-XRT* observations were performed in windowed mode, allowing study of timing properties of the source. We performed standard analysis with *xrtpipeline* and barycentered data prior to lightcurve extraction. During several observations countrate was as high as 280 cts s^{-1} , therefore we excluded one or few brightest columns depending on countrate, in order to suppress effects caused by photon pile-up. Photons with energies below 0.8 keV and above 10 keV were also filtered out. Long-term lightcurves and spectra were obtained from UK Swift Science Data Centre at the University of Leicester (Evans et al. 2009).

4 ANALYSIS

4.1 Outburst

First detection of the source by *Swift-BAT* (Krimm et al. 2014) occurred at March 9, 2014 (MJD 56725, we will refer to this date as τ_0). Outburst profile in hard X-rays (15–50 keV) featured fast rise with tenfold intensity increase over ten days, nearly flat-top peak ($\tau_0 + 10..+15$ days) followed by abrupt flux decrease by 30% over the course of two days. After this, the source demonstrated gradual decline interrupted by flaring activity at $\tau_0 + 50..+70$ days. At $\tau_0 \approx +86$ days a sharp dip occurred in the *Swift-BAT* lightcurve. After the cease of the outburst source remained active with flux about 5–15 mCrab.

Adding data from *MAXI* to the *Swift-BAT* hard X-ray lightcurve gives us another insight on the outburst evolution as shown in Fig. 1 – comparing fluxes in soft and hard bands (for 2–4 keV band we took a $1.67 \text{ counts s}^{-1}$ as a reference value for Crab, corresponding value for 15–50 keV band is $0.22 \text{ cts cm}^{-2} \text{ s}^{-1}$) one can see that the soft component

obviously lags hard emission in the beginning of the outburst but then starts to grow and ends up dominating during the flaring period as well as during hard dip. Lower subplot of Fig. 1 shows evolution of hardness ratio (3–10 keV/0.8–3 keV) measured by *Swift-XRT*. Right after the peak of hard emission one can see the decline of hardness, also indicating appearance of the thermal component. Detailed analysis of the spectral evolution during the outburst will be presented in Bykov et al., (2018) in preparation.

Fortunately, *NuSTAR* observation triggered by Miller et al. (2015) were carried right at the transition between hard and soft states, thus giving us unique possibility to study processes that happens during HIMS.

4.2 NuSTAR observation

NuSTAR observed GRS 1739–278 for nearly 30 ks of net exposure right after the hard X-ray peak (at $\tau_0 \approx +18$, see Fig. 1). Earlier, Miller et al. (2015) shown that the average spectrum of this observation is well described by relativistic reflection models such as *relxill* (García et al. 2014; Dauser et al. 2014, 2016) with accretion disk that reaches remarkably close to the black hole innermost stable circular orbit (ISCO), with disk inner edge radius upper estimate being $R_{\text{in}} = 5^{+3}_{-4} GM/c^2$ (Miller et al. 2015). They also noted that no additional thermal component was needed in order to describe *NuSTAR* energy spectrum probably due to the low disk temperature and high absorption.

Given the 96.9 minute orbital period of *NuSTAR*, observation is divided in 13 intervals separated by Earth occultations, as shown in Fig. 2. We denoted these intervals with roman numerals, from **I** to **XIII**. From the lightcurve it is clear, that the source flux increased throughout observation from ≈ 145 up to ≈ 170 counts per second. The spectrum also altered, with hardness (defined as ratio of

count rates $R_{3-10\text{ keV}}/R_{10-78\text{ keV}}$) had been growing monotonically from 2.7 to 3.1.

4.2.1 Continuum evolution

To get better view on the evolution of continuum emission we fitted all individual interval spectra using **XSPEC** package (Arnaud 1996) with absorbed **xillver** (García et al. 2013) model (**const*phabs*xillver**). This model describes reflection of incident radiation from ionized slab of matter. The spectrum of incident radiation are assumed to be power-law with exponential cutoff. We picked **xillver** model over the **relxill** for separate intervals analysis because we wanted to describe the changes in the continuum emission making no assumptions on the system geometry.

Spectra from two *NuSTAR* modules of each interval were fitted simultaneously with free cross-calibration constant between modules. Before fitting, spectra were grouped in order to have at least 100 counts per bin, channels above 60 keV were ignored. We choose to fix interstellar absorption at $N_H = 2.15 \times 10^{22} \text{ cm}^{-2}$ as was found by joint *XMM-Newton*/*NuSTAR* observation during the low luminosity state (Fuerst et al. 2016). Element abundances were taken from Wilms et al. (2000) and cross-sections from Verner et al. (1996). Relative iron abundance were fixed at $A_{Fe} = 1$, ionization parameter at $\xi = 3.2$ and inclination at 35 degrees, in consistency with Miller et al. (2015) results obtained with different spectral models. Although in **xillver** there is no relativistic broadening of Fe $K\alpha$ emission line no significant residuals in 5–8 keV region are seen, mainly because of limited statistics in per interval spectra. Resulting fits are of satisfactory quality with $\chi^2_{red.} \approx 1.05$.

Examination of the best-fit parameters (see Fig. 3) confirms that the spectrum softens during the observation and the cut-off energy decreases.

4.2.2 Constrains on movement of the inner parts of accretion disk

Spectra of single intervals have not enough statistics to constrain change of Fe-line profile and, hence, to determine whether the disk inner boundary is moving during observation. To increase statistics, we split whole observation into three major pieces, with first made by intervals **I–IV**, second by **V–IX** and third by **X–XIII** and extracted 4–78 keV spectra. We chose to group them in order to have at least 100 counts per bin and then we fitted them (excluding data between 5–10 keV) with simple **phabs*cutoffpl** model, using, once again, $N_H = 2.15 \times 10^{22} \text{ cm}^{-2}$.

Now, plotting the ratio of this fit to initial spectra (see Fig. 4) one can see that both strong features - i.e. Fe-line complex at 5–9 keV and Compton hump around 30 keV are seemingly stable. Additionally, we estimated the equivalent width of Fe $K\alpha$ emission line in this three parts - we approximated 4–78 keV spectra with 10–30 keV range being ignored (to neglect the Compton-hump contribution) with model consisting of absorbed cut-off powerlaw and gaussian. Equivalent width of the gaussian component is around 0.175 keV and remains constant along the observation within error margins, although it is possible that the quality of data is not enough to trace the real change. Therefore we can

conclude, that there is no drastic change in position of inner disk boundary between parts of observation.

4.2.3 Broadband average spectrum

There is a 1.3 ks part of *Swift-XRT* snapshot (ObsId: 00033203003) that coincides with *NuSTAR* observation. Extension of an energy range to 0.8–78 keV allows one to search for thermal emission associated with the cold inner disk with $kT \sim 0.1\text{--}0.4$ keV (such as were found in other BHCs, see (Miller et al. 2006a,b; Parker et al. 2015, et.c)).

We extracted *Swift-XRT* spectrum using only zero-grade events, grouped it to has at least 30 counts per bin and added 3% systematic error. Similar grouping were applied to *NuSTAR* data.

Since the average spectrum has much better statistics we applied more sophisticated **relxillp** spectral model that describes reflection of emission, produced by point source located on the rotation axis above the Kerr black hole, from the relativistic accretion disk. We used latest available version of **relxillp** package (v1.0.2). Jet foundation are often thought to be responsible for this type of “lamp-post” geometry. Among the parameters of a model several are of a particular interest, namely h - height of a point source above the black hole illuminating the accretion disk and R_{in} - disks inner radius. We selected this model for several reasons - first, Miller et al. (2015) found that it matches *NuSTAR* data well. Also, during the 1996 outburst source was detected at radiowaves, possibly indicating jet activity. For spectral fitting we used **migrad** minimizer from **MINUIT** package (James and Roos 1975), and in order to estimate errors we employed a large MCMC chain.

Interestingly, instead of surplus thermal component we found a lack of the soft emission - usage of $N_H = 2.15 \times 10^{22} \text{ cm}^{-2}$, measured in the low state (Füerst et al. 2016) led to worse fits with systematic negative residuals below few keV. Therefore, we left N_H free during the fit. Obtained value of $2.64 \times 10^{22} \text{ cm}^{-2}$ is higher than one measured by Füerst et al. (2016). This can be possibly accounted to a presence of disk outflow, caused by severe X-ray irradiation.

Obtained upper limit on the accretion disk truncation radius - $R_{in} < 9GM/c^2$ (90% confidence limit) is similar to the value from Miller et al. (2015), height of the source above the accretion disk is in agreement too (see Tab. 1 for obtained parameters). Some discrepancy seen in the parameters of accretion disk - e.g. inclination, ionization parameter and Fe-abundance, it can be caused by a broader energy range used in this study. As it can be seen from Fig. 5 there are no significant residuals in lower-energy part of the spectrum, therefore thermal emission from accretion disk is too weak or too cold to detect.

Total unabsorbed flux in 0.1–100 keV band is about $1.4 \times 10^{-8} \text{ erg s}^{-1} \text{ cm}^{-2}$ which translates to a luminosity of $1.1 \times 10^{38} \text{ erg s}^{-1}$ for the 8 kpc distance. Typical luminosity at which BHCs change from LHS to HIMS is about $0.1 L_{Edd} = 1.2 \times 10^{37} (M/M_\odot) \text{ erg s}^{-1}$, although we should note that there is significant scatter in this value. Therefore one can put a rough lower estimate on the black-hole mass as $9 M_\odot$, which is reasonable.

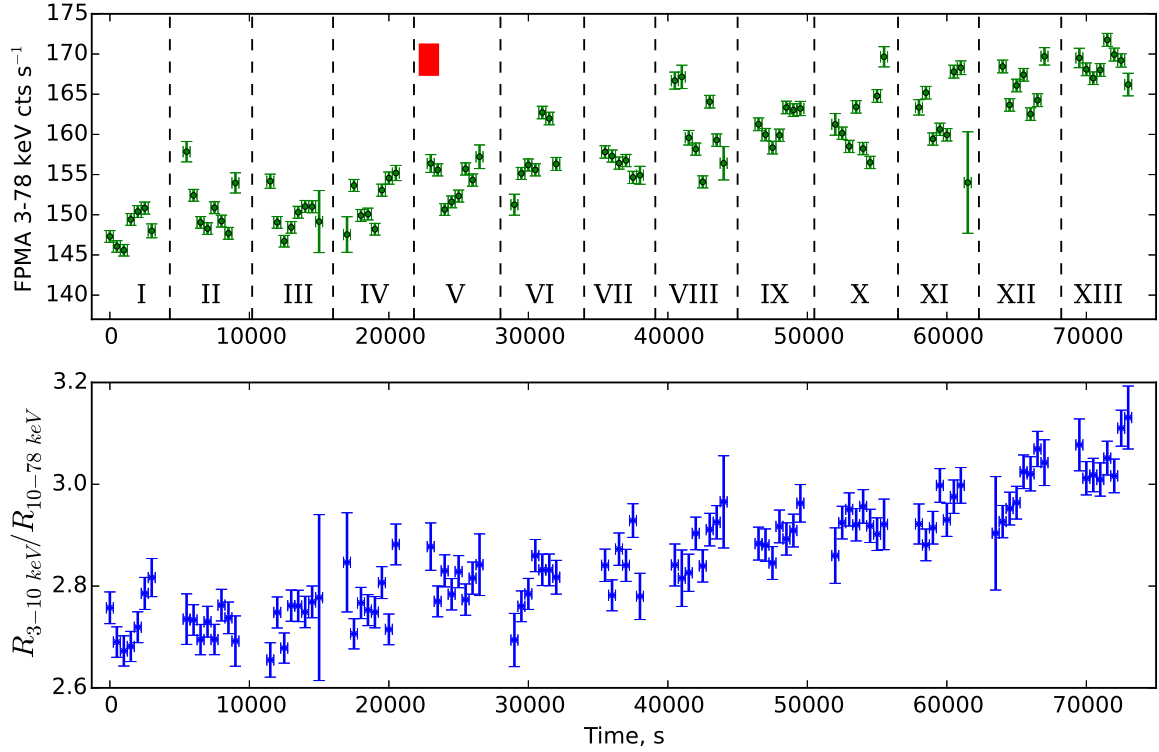


Figure 2. Upper panel: countrate of *NuSTAR* FPMA in 3–78 keV band. We enumerated intervals of uninterrupted observations with roman numerals. Red square shows time of simultaneous *Swift-XRT* observation (ObsId: 00033203003, second part). Bottom panel: evolution of hardness during observation

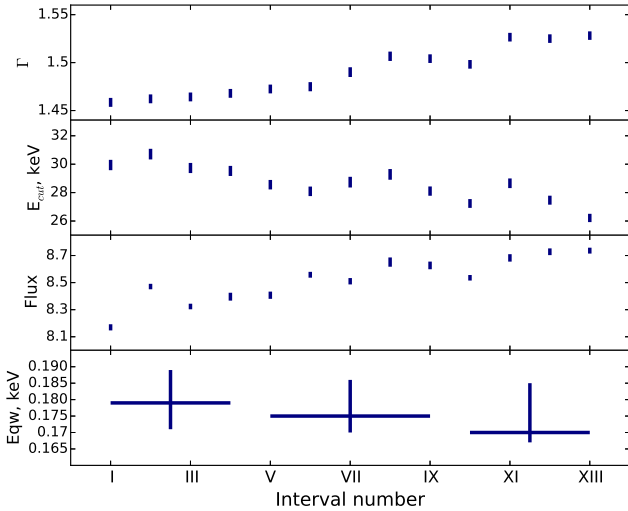


Figure 3. Parameters of continuum emission in intervals. From upper to lower: *xillver* powerlaw slope, cutoff energy and flux in 3–60 keV band $\times \text{erg s}^{-1} \text{cm}^{-2}$ (see sec.4.2.1). On the bottom panel we present Fe $K\alpha$ line equivalent width obtained with *phabs*×(*cutoffpl* + *gauss*) model (see sec.4.2.2).

5 TIMING ANALYSIS

Variability properties of different types of X-ray binary systems are usually described in terms of the power spectrum. Power spectrum of the BHC systems in LHS/HIMS typi-

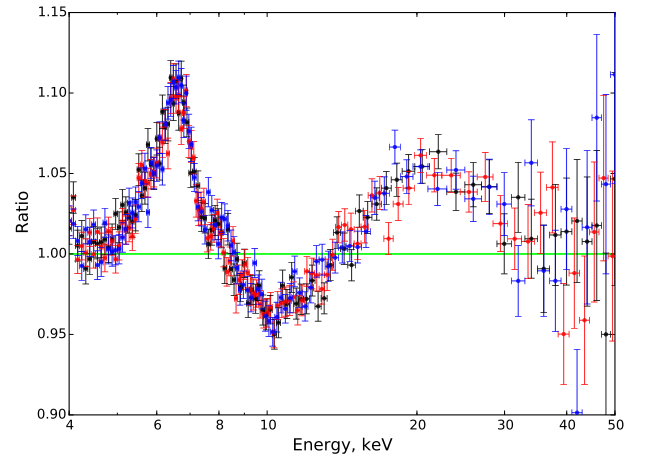


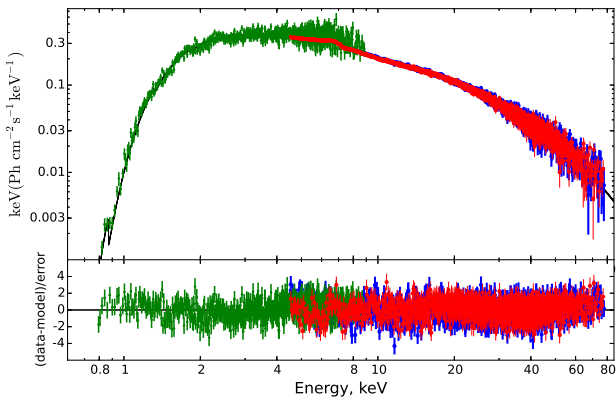
Figure 4. Ratio of *NuSTAR* FPMA spectra to *phabs*×*cutoffpl* model. In black - data from intervals I–IV, in red from V–IX and in blue from X–XIII.

cally can be described as a combination of a band-limited noise and one or few narrow Lorentzian functions, representing QPOs (see, e.g. Terrell 1972; Belloni and Hasinger 1990; Homan and Belloni 2005, e.t.c). Properties of this components and correlations between them, in principle, may be used to discriminate between different models, proposed for generation of X-ray emission in BHC.

Although power spectra analysis is by far the most pop-

Table 1. Best-fit parameters of `phabs*relxilllp` model

Parameter	Value
$N_H, 10^{22} \text{ cm}^{-2}$	$2.64^{+0.05}_{-0.03}$
$h, GM/c^2$	$22.3^{+0.6}_{-4.3}$
$a, cJ/GM^2$	$0.73^{+0.26}_{-0.23}$
$incl, \text{deg}$	$22.1^{+2.9}_{-2.0}$
$R_{in}, ISCO$	$1.05^{+1.73}_{-0.02}$
Γ	$1.40^{+0.01}_{-0.01}$
$\log \xi$	$3.52^{+0.05}_{-0.07}$
A_{Fe}	$3.0^{+0.6}_{-0.3}$
E_{cut}, keV	$26.3^{+0.3}_{-0.5}$
R_{refl}	$0.42^{+0.03}_{-0.03}$
$N_{FMPA}, \times 10^{-2}$	$1.49^{+0.09}_{-0.03}$
C_{FMPB}	$1.017^{+0.002}_{-0.001}$
$C_{Swift-XRT}$	$1.04^{+0.01}_{-0.01}$
$\chi^2_{red.}$	1.1 =
	= 3366.21/3062 d.o.f

**Figure 5.** Fit of composite *Swift*-*XRT*/*NuSTAR* spectrum by `phabs*relxilllp` model. Green, red and blue points correspond to *Swift*-*XRT*, *NuSTAR* FPMA and FPMB, correspondingly.

ular, more sophisticated methods, such as coherence function or phase-lag were successfully applied to infer physical properties of accretion flows. For example, using a measured time-lag between the soft and hard emission, which has a complex behavior with the frequency Nowak et al. (1999a) constrained geometrical size of the accretion flow.

In the following section we present analysis of the GRS 1739–278 timing properties and their evolution during the 2014 outburst.

5.1 Power spectrum

We split *NuSTAR* observation of the GRS 1739–278 2014 outburst on 13 continuous intervals separated with ~ 0.7 hr intervals when the source was occulted by Earth. The continuous intervals have duration about 3 ks, see Table 2. Since *NuSTAR* detectors operate in the photon counting mode, data can be reduced to the lightcurve with time resolution up to $2\mu\text{s}$. For our analysis we extracted lightcurves with 0.01 s temporal resolution in a few energy bands (3–78, 3–5, 5–8, 8–15, 15–78 keV), which allows us to examine $\sim 3 \times 10^{-3}$ –

50 Hz frequency range. As it was mentioned above, this is a frequency band which usually contains low frequency QPOs and a broad band noise (Wijnands and van der Klis 1999). We produced power spectrum for each interval of *NuSTAR* observation using 3–78 keV lightcurves. All power spectra have a form of a plateau ($P(f) \propto \text{const}$) on the low frequencies, transforming at the frequency ≈ 0.1 Hz in to the power law with the slope $\rho \approx -1.6..-2.0$ and to the Poisson noise plateau at the frequencies above few Hz. Also a prominent QPO at the frequencies 0.3–0.7 Hz and its second harmonic are present. Typical power spectrum (with subtracted Poisson noise, see text below) of a single interval is shown in Fig. 6.

In order to quantitatively characterize properties of broad band noise and QPOs we approximate each obtained power spectra with the following analytical function:

$$P(f) = n(1 + (f/f_{lb})^4)^\alpha + \frac{s_1}{(f - f_{QPO})^2 + (f_{QPO}/Q_m)^2} + \frac{s_2}{(f - 2f_{QPO})^2 + (2f_{QPO}/Q_m)^2} + P_{\text{poiss}} \quad (1)$$

Where f_{lb} - broad noise break frequency, f_{QPO} and Q_m - centroid of the QPO and its quality correspondingly and P_{poiss} - represents mean power of the variations caused by the counting statistics and dumped by the dead-time. In this function first component represents plateau with the break, second two components describe QPO main harmonics and its overtone, last component represents Poisson noise. We take that the quality of the QPO second harmonic is equal to the QPO peak quality. Further in the text will mention this models as standard.

In order to properly determine all parameters one have to know the shape and normalization of Poisson noise component, which depend on countrate and dead time and in principle can be described with analytical functions (see, e.g., Vikhlinin et al. 1994; Zhang et al. 1995). *NuSTAR* detectors are subject to non-paralyzing dead time with characteristic timescale $\tau \approx 2.5$ ms (Bachetti et al. 2015), in our case effects from dead-time already can be observed in power spectra at frequencies above 20 Hz. Bachetti et al. (2015) noted that *NuSTAR* dead-time has a complex dependence on the energy of registered photons, and therefore it is hard to create analytical model for the power spectrum of Poisson noise. To avoid this problem they proposed to use cross-spectrum (or shortly cospectrum) for analysis of *NuSTAR* data instead of power spectrum. They determine cospectrum as a real part of the cross product of Fourier function of lightcurves obtained from two *NuSTAR* detectors

$$P(F) \approx \langle \text{re}(F_{\text{FPMA}}^*(f)F_{\text{FPMB}}(F)) \rangle \quad (2)$$

where $P(f)$ is the estimation of the studied source intrinsic variability power spectrum, $F_{\text{FPMA[B]}}$ - Fourier function of a light curve from FPMA[B] module, * - stands for complex conjugation. This method is based on the following assumption: signals produced by an observed source on two detectors are identical and have no time lag and therefore their Fourier functions are also identical and have zero phase shift, in contrast, signals independent for two detectors (like counting statistics) have random phase shifts. It follows that for independent signals the average real part

of the cross product tends to zero due to the random phase shift, i.e. Poisson noise is eliminated.

Huppenkothen and Bachetti (2017) shown that the cospectrum value in each frequency bin is distributed with Laplace probability density function (PDF) if it is derived from two normally distributed random independent series (see, e.q. 14 in Huppenkothen and Bachetti 2017):

$$p(C_j|0, \sigma_x \sigma_y) = \frac{1}{\sigma_x \sigma_y} \exp\left(\frac{-|C_j|}{\sigma_x \sigma_y}\right) \quad (3)$$

Where C_j - cospectrum of two *uncoherent* series measured in the j -th frequency channel and σ_x, σ_y - are second momenta of the initial normal distributions (therefore they are equal to the square of the power spectra in corresponding frequency channel for each time series). If signals used for the cospectrum estimation have identical power spectra then $\sigma_x = \sigma_y \approx |F_{\text{FPMA}}|$. We, therefore, see that to determine proper likelihood function which can be used to approximate cospectra with analytical functions, one still has to know Poisson noise level. It is also worth noting, that source count-rate and total count-rate are usually slightly differs for two *NuSTAR* modules making amplitudes of counting-statistic and dead-time not equal. Taking all this arguments into consideration we decided to use standard power spectrum analysis in our study.

Since we used relatively large time binning (10 ms) to extract lightcurves from *NuSTAR* data and also usually considered variability at frequencies below 10 Hz, we assumed that the only effect from the dead-time is lowering of the constant Poisson noise level on some $(1 - 2\nu\tau_d)$ factor, where ν is total count rate for detector and τ_d is a dead time (Vikhlinin et al. 1994; Zhang et al. 1995). Since the dead-time is not constant along energy, we measured modified Poisson level for each extracted data-set separately.

We did not try to find any high frequency QPOs, since the typical HF QPO (centroid frequency 100–400 Hz, amplitude $\approx 10\%$ and quality $Q \approx 2$ –10) is indiscernible over the Poisson noise with the obtained count-rate and duration of the observation. ”more text here :”

We found that the QPO frequency evolves with time see Table 2 and Figure 6. The QPO frequency correlates with the *NuSTAR* flux and photon index, similar to many other black hole and neutron star binary systems (see, e.g., Vignarca et al. 2003; Pottschmidt et al. 2003). On the other hand we see, that the QPO amplitude remained stable during the first half of the observation, and started to grow in the second part.

We also inspect power spectra in soft (3–5 keV) and hard (15–78 keV) energy bands. We found that the QPO amplitude is smaller in the soft band, while amplitude of its harmonic is bigger. The ratio of the power in the QPO and its harmonic for hard and soft energy bands is presented in Fig. 7. It follows that the QPO profile in time domain, such as was found by Ingram and van der Klis (2015) in GRS 1915+105, differs in the hard and soft X-ray bands. Following Ingram and van der Klis (2015) we tried to extract QPO profile by segregating the coherent part (Fourier signal with conserving phase shift relative to the signal on QPO frequency) between the QPO and its harmonics, however no significant coherence was detected above the noise level. It indicates that the QPO profile was not stable during the observation, in contrast with the result obtained by

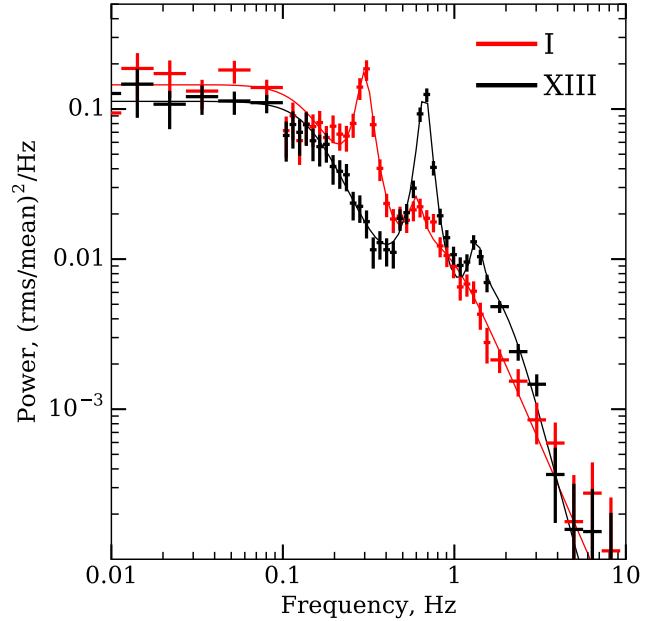


Figure 6. Power spectrum of the GRS 1739–278 obtained with *NuSTAR* data at the beginning (red crosses) and at the end (black crosses) of the observation. Poisson noise is subtracted.

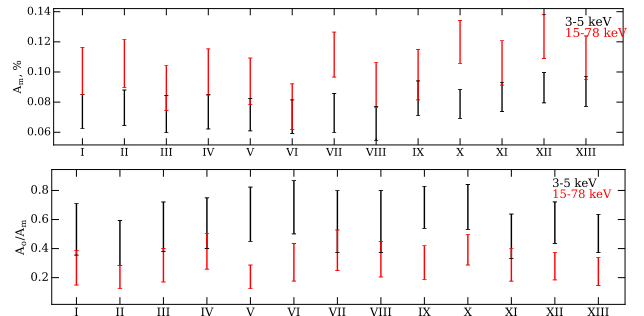


Figure 7. On top panel: amplitude of the QPO harmonic in % of mean count-rate, on the bottom panel: ratio of the total power in the QPO and its second harmonic measured for the lightcurves obtained in 3–5 keV and 15–78 keV energy bands.

Ingram and van der Klis (2015) for GRS 1915+105 with *RXTE* observatory data.

In some intervals QPO subharmonics, centered approximately at 1/2 of the QPO centroid frequency, is clearly observed in the cospectra (see examples on Fig. 8, red crosses) (namely I, II, IV, V, VI sets). In order to observe QPO with better significance we stacked several cospectra, frequency of each cospectrum was scaled in such a way to conserve QPO centroid at 0.3 Hz. Obtained “tracked” cospectrum is presented on Fig. 8. The subharmonics seems to roam around the 1/2 QPO frequency, therefore we were not able to obtain it with a large significance on the tracked cospectrum.

It should be noted that the changes in the QPO centroid position during the interval may contribute to the observed quality factor Q . We can estimate the derivative of the QPO centroid position with time (by approximating $f_{\text{QPO}}(\text{time})$

Table 2. Evolution of the Fourier and energy spectrum properties through the *NuSTAR* observation in the 3–78 keV energy band.

Interval	T_{start} , MJD	Expo, s	f_{br} , $\times 10^{-2}$, Hz	f_{QPO} , Hz	Q_m ,	A_m , %	A_o , %	rms %	Γ	E_{cut} , keV
I	56742.68	3386	$8.9^{+2.2}_{-2.3}$	0.30 ± 0.01	15^{+5}_{-3}	$7.5^{+0.9}_{-1.0}$	$2.7^{+0.8}_{-0.9}$	26 ± 1	1.459 ± 0.005	29.9 ± 0.4
II	56742.75	3388	$7.8^{+2.0}_{-1.8}$	0.31 ± 0.01	13 ± 3	$7.9^{+1.0}_{-0.9}$	$2.7^{+0.8}_{-0.9}$	26 ± 1	1.462 ± 0.005	30.7 ± 0.4
III	56742.82	3392	$8.2^{+2.4}_{-1.9}$	0.34 ± 0.01	12^{+3}_{-2}	$7.7^{+0.9}_{-0.8}$	$3.9^{+0.9}_{-0.8}$	26 ± 1	1.464 ± 0.005	29.7 ± 0.4
IV	56742.88	3389	$8.3^{+2.0}_{-1.8}$	0.35 ± 0.01	15^{+4}_{-3}	7.6 ± 0.9	$3.2^{+0.7}_{-0.8}$	26 ± 1	1.468 ± 0.005	$29.5^{+0.4}_{-0.3}$
V	56742.95	3389	$6.9^{+1.6}_{-1.4}$	0.39 ± 0.01	13^{+4}_{-3}	7.4 ± 0.8	$4.3^{+0.8}_{-0.9}$	26 ± 1	1.473 ± 0.005	28.6 ± 0.3
VI	56743.02	3136	$7.5^{+1.9}_{-1.5}$	0.41 ± 0.01	17^{+5}_{-3}	$6.9^{+0.9}_{-0.8}$	$3.8^{+0.7}_{-0.8}$	26 ± 1	1.475 ± 0.005	28.1 ± 0.3
VII	56743.09	2771	$9.7^{+2.7}_{-2.2}$	0.43 ± 0.01	12^{+3}_{-2}	7.4 ± 0.9	3.6 ± 0.9	26^{+2}_{-1}	1.500 ± 0.005	28.7 ± 0.4
VIII	56743.15	3387	$5.8^{+1.4}_{-1.5}$	0.46 ± 0.01	11^{+3}_{-2}	7.9 ± 0.9	$4.2^{+0.9}_{-0.8}$	27 ± 2	1.507 ± 0.005	29.3 ± 0.4
IX	56743.22	3392	$7.1^{+1.6}_{-1.4}$	0.50 ± 0.01	12^{+4}_{-3}	7.9 ± 0.8	4.3 ± 0.8	26 ± 1	1.504 ± 0.005	28.1 ± 0.3
X	56743.29	3390	$7.0^{+1.7}_{-1.6}$	0.53 ± 0.01	13^{+3}_{-2}	8.7 ± 0.7	$4.5^{+0.7}_{-0.8}$	25 ± 1	1.498 ± 0.005	27.2 ± 0.3
XI	56743.35	3382	(6.7 ± 1.5)	0.57 ± 0.01	13 ± 3	$9.1^{+0.8}_{-0.7}$	4.0 ± 0.8	25 ± 1	$1.527^{+0.004}_{-0.005}$	28.7 ± 0.3
XII	56743.42	3386	$6.7^{+1.8}_{-1.4}$	0.63 ± 0.01	14^{+3}_{-2}	$9.5^{+0.8}_{-0.7}$	4.4 ± 0.7	26^{+2}_{-1}	1.525 ± 0.004	27.5 ± 0.3
XIII	56743.49	3391	$7.5^{+1.7}_{-1.5}$	0.67 ± 0.01	15 ± 3	9.6 ± 0.7	4.2 ± 0.8	25^{+2}_{-1}	1.528 ± 0.004	26.2 ± 0.3

In Table f_{br} is broad band noise break frequency, f_{QPO} is QPO centroid frequency, Q_m is QPO main harmonic quality (ratio of its centroid frequency to its width), A_m - total power in the QPO main harmonic in % of mean countrate, A_o is total power in the QPO second harmonic in % of mean countrate, rms - total amplitude of variations in the % of mean countrate, Γ - powerlaw photon index, E_{cut} - powerlaw cutoff energy. Parameters Γ and E_{cut} were obtained from spectra of individual intervals with *xilver* model (see sec.4.2.1).

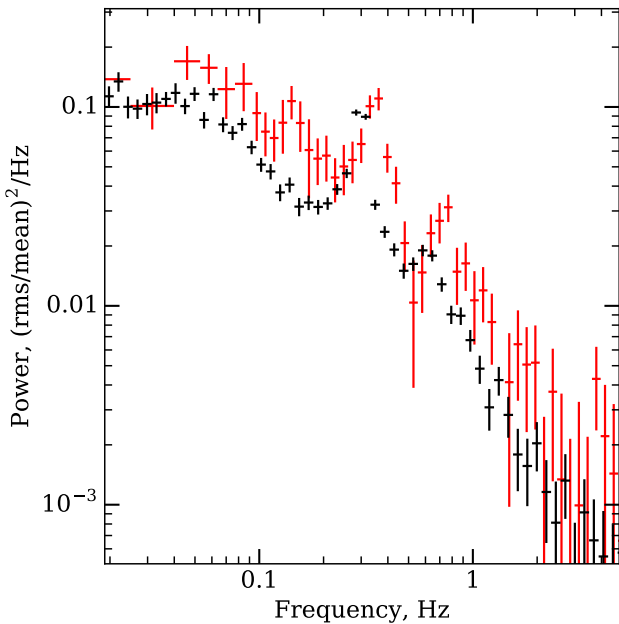


Figure 8. Cross-spectrum of the observations, obtained by scaling frequency to conserve QPO position. Black crosses obtained from the all intervals, while red crosses are from interval IV in which QPO subharmonics was most prominent.

with the straight line), which appears to be $\dot{f}_{QPO} \approx 5.0\text{--}6.5 \times 10^{-6} \text{ Hz s}^{-1}$. During an interval with the duration $\tau = 3000 \text{ s}$ observed QPO drift will broaden the perfect periodic signal located at $f_{QPO} = 0.3 \text{ Hz}$ up to the quality factor $Q \approx f_{QPO}/(\dot{f}_{QPO}\tau) \approx 17$, which is of order of the Q estimations obtained from the observations with standard model (described with eq.1). In order to better estimate the QPO

quality factor, we split each of the 13 intervals in sets of 82 s long time-series. After that, for each of 13 intervals, we fitted obtained power spectra simultaneously with new model in which we assume that QPO frequency linearly growing with time. The model has the same form as standard with f_{QPO} substituted with $f'_{QPO} = f_{QPO} + (t - t_{mid})\dot{f}_{QPO}$, where f_{QPO} is the free parameter and t_{mid} , \dot{f}_{QPO} are the middle time of the i -th 82 s interval and QPO centroid frequency measured with standard model correspondingly. Inside each data set we obtained the QPO centroid changing speed consistent with the estimation obtained from the general trend ($\approx 2\text{--}9 \times 10^{-6} \text{ Hz s}^{-1}$), nevertheless the median quality factor, obtained in this model appears to be ~ 14.3 - i.e. compatible with the previous estimations made with standard model (see Table 2). It should be noted that the estimation of the QPO quality factor is restricted by the width of fast Fourier transform frequency bins, which is $1/T$, where T - is a duration of separate series used for fitting, in our case $T = 82 \text{ s}$, and QPO width is limited at $1/T = 0.012 \text{ Hz}$ (we can not discriminate $Q > 25$).

From the shape of the energy and Fourier spectrum we concluded that the system is in the hard intermediate state and observed low frequency QPO (LF QPO) is of type C.

5.2 Coherence

Vaughan and Nowak (1997)(hereafter V97) suggested to use coherence between different energy bands in order to obtain additional information from the source variability. Coherence measure the similarity between two signals and can be computed with the following expression:

$$C(f) = \frac{|\langle F_s(f)^* F_h(f) \rangle|^2 - n^2}{\langle |F_s(f)|^2 \rangle \langle |F_h(f)|^2 \rangle} \quad (4)$$

where $F_h(f)$ and $F_s(f)$ are Fourier function (corrected for the Poisson noise components) of the observed time series

in hard and soft bands, correspondingly, n^2 - product of the power in uncorrelated components, connected with counting statistic, divided by the number of used series (V97). Coherence should be computed for the number of independent time series, therefore we separated each of the available uninterrupted time intervals on several shorter parts, 82 s long each.

Coherence is very similar to cospectrum, but instead of tracking signals with zero phase shifts, it tracks all signals with arbitrary conserved phase shift - i.e. Fourier harmonics of the signals may delay each other but be coherent (which means that Fourier functions $F_h(f)$ and $F_s(f)$ are related by linear transformation V97).

Different models of the XBs variability generation suggest that the signals in two energy bands can be partially independent, while the shape of the power spectra is conserved. It appears that in many sources coherence between soft and hard X-ray bands is close to unity (Nowak et al. 1999a; Wijnands and van der Klis 1999), however there also were indications on complex picture of the coherence in particular state of some systems (Ji et al. 2003), or drop in coherence between particular energy bands (e.g. in GX 339–4 Vaughan and Nowak 1997). See also discussion in the V97 for the theoretical prediction on the coherence for different models.

Following V97, we estimated coherence of GRS 1739–278 light-curves obtained in different soft and hard energy bands. Since for the timing analysis we use *NuSTAR* data, covering 3–78 keV energy band, we adopted following energy bands for our analysis: 3–5 keV, 5–8 keV, 8–15 keV and 15–78 keV. This partition of the *NuSTAR* energy band pursues the following idea: the energy spectrum of GRS 1739–278 can be described with the two major components - powerlaw continuum and reflection features i.e. fluorescent Fe K α line and Compton hump. In 5–8 keV band there is a contribution of the prominent Fe K α line, given the equivalent width 0.2 keV it provides about 5% of flux. In 8–15 keV energy band we expect only the power law component to be present. Compton hump, another reflection features, is confined in 15–78 keV energy band.

As it was mentioned above the *NuSTAR* detectors have complex dead-time depending on energy, coherence computed from one detector is subject to the dead-time crosstalk effects (which should make random processes more coherent). In order to eliminate this effects in coherence estimation, following the recipe suggested in Bachetti et al. (2015) for cospectrum, for the numerator in Eq. 4 we used cross-products of the Fourier functions of lightcurves obtained from the different modules - e.g. correlations of the lightcurve obtained in the soft band on the FPMA module with the lightcurve in the hard band obtained on the FPMB module and vice versa. In the obtained cross-product effects of dead-time crosstalk are significantly dumped. We also used cospectrum obtained for each energy band as the estimation for the denominator in Eq. 4. The n^2 component was computed as it is suggested by V97, however for the Poisson noise components power estimation we used mean value of the power spectra in the 5–15 Hz range, assuming that Poisson noise dominating intrinsic source variability and is constant along frequencies.

Wijnands and van der Klis (1999) shown that primary features of the power spectrum of the XBs in low-hard and

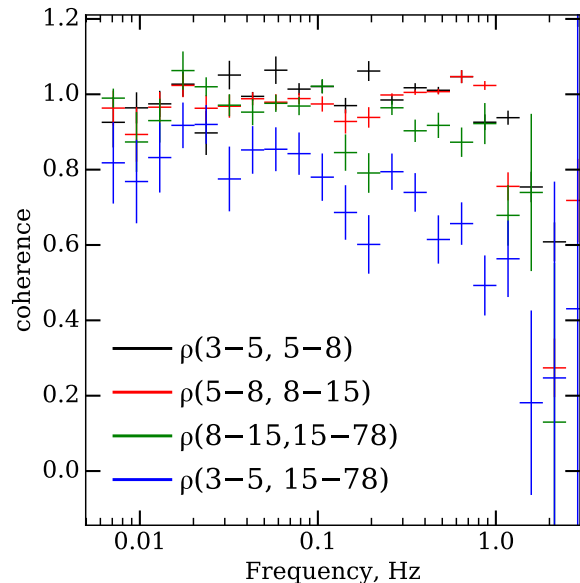


Figure 9. Coherence between different energy bands: red crosses between 3–5 and 5–8 keV, green crosses between 5–8 and 8–15 keV, blue crosses between 8–15 and 15–78 keV, black crosses between 3–5 and 15–78 keV.

high intermediate states are evolving simultaneously, i.e. flat top broad band noise break frequency and QPO centroid frequency are connected with the relation $f_b \approx 0.3f_{\text{QPO}}$. Bearing in mind aforementioned property of the power spectrum and small scatter in the f_b/f_{QPO} in our data, to improve significance of the coherence measurements, we stacked all 13 separate intervals of the observation, scaling their frequencies to preserve QPO position. We assumed that the coherence in each tracked frequency channel is preserved along the observation.

The coherence between hard and soft energy bands at frequencies up to ~ 3 Hz is presented in Fig. 9. We found that coherence in the adjacent energy bands is close to unity, with mean values in 0.01–1 Hz frequency band being 1.0 ± 0.05 , however for the 3–5 and 15–78 keV energy bands the coherence is significantly lower, see Fig. 9. It is on the nearly constant level of ≈ 0.85 in the 5×10^{-3} –0.1 Hz frequency band and drops down above this frequency.

5.3 Phase lags

From the definition of the coherence (see eq. 4) it follows that signals have roughly constant phase shifts between their Fourier functions in each frequency bin where they are coherent. Following Vaughan and Nowak (1997) we estimated phase lag as an angle of mean product of the light curves Fourier harmonics from one energy bands to the conjugated Fourier harmonics of the second energy band.

$$\delta\phi(f) = \arctan \left(\frac{\text{Im}(\langle F_s^*(f) F_h(f) \rangle)}{\text{Re}(\langle F_s^*(f) F_h(f) \rangle)} \right) \quad (5)$$

For the error estimation we used Uttley et al. (2014) approach, therefore $\Delta\delta\phi \approx \arctan(\Delta\gamma^2/\gamma^2)$, where γ^2 - esti-

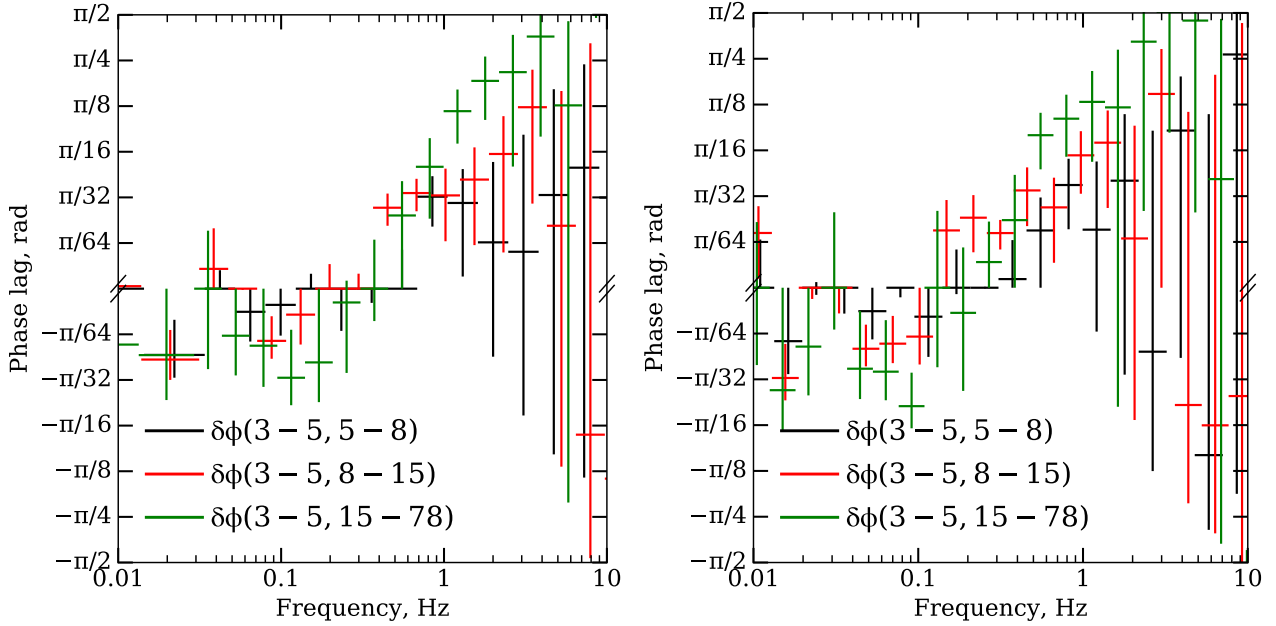


Figure 10. Phase lag between the soft (3–5 keV) and hard (5–8; 8–15; 15–78 keV) energy bands in GRS 1739–278. On the left panel - phase lag spectrum obtained from *NuSTAR* observations by stacking all data, on the right panel same spectrum with tracked frequency (frequency for each separate light-curve segment was scaled such a way to conserve QPO centroid at 0.3 Hz).

Table 3. QPOs detected in *Swift-XRT* observations

Segment	t_{mean} days from τ_0	f_{QPO} , Hz	QPO rms , %	Total rms , %	Type
03	17.9	0.37 ± 0.01	9 ± 2	28 ± 3	C
04	21.9	2.17 ± 0.03	8^{+1}_{-2}	14^{+2}_{-1}	B
05	26.8	$1.67^{+0.03}_{-0.04}$	8 ± 1	17^{+6}_{-3}	B
06	31.8	5.05 ± 0.09	4^{+2}_{-1}	11^{+2}_{-1}	B
07	36.0	$2.52^{+0.07}_{-0.08}$	7^{+1}_{-2}	15^{+3}_{-2}	B
08	39.8	$5.10^{+0.16}_{-0.14}$	5 ± 1	12^{+3}_{-2}	B
09	46.6	$2.17^{+0.02}_{-0.04}$	7^{+2}_{-1}	17^{+4}_{-3}	B

mation of the coherence, and $\Delta\gamma^2$ is coherence error estimation. It should be noted that this estimation of the error is build on the assumption that each product $\langle F_s^*(f)F_h(f) \rangle$ can be represented as a sum of randomly (for uncoherent signals) and particularly oriented (for coherent signals) vectors with constant length on complex plane, while it can be shown that, at least for uncoherent signals, the length of this vectors is also random variable with Laplace distribution (Huppenkothen and Bachetti 2017).

We computed the phase lag spectrum with two approaches - with and without QPO centroid frequency tracing (see right and left panels of Fig.10 correspondingly). It appears that in the 0.1–3 Hz frequency band positive (hard) lag is present, on the frequencies below 0.1 Hz there are indication on the negative (soft) lag. Observed phase lag corresponds to the delay times between soft and hard photons ~ 0.1 s for frequencies above 0.1 Hz and $-0.1..-1$ s for frequencies below 0.1 Hz.

Phase lag in different BHC system is being investigated by many authors (see, e.g. Vaughan and Nowak 1997; Malzac et al. 2003; Reig et al. 2006;

Gandhi et al. 2010; Böck et al. 2011; Muñoz-Darias et al. 2011; Cassatella et al. 2012; Méndez et al. 2013; Yan et al. 2017; De Marco et al. 2017; Zhang et al. 2017; van den Eijnden et al. 2017; Reig et al. 2018, and others). It was found that for stellar mass black holes phase lag in the frequency range occupied by flat-top noise and LF QPOs are usually hard and can be described with the power law $\Delta\phi/(2\pi f) = \Delta\tau \propto f^{-0.7}$ with some features. Zhang et al. (2017) shown that the phase lag at the QPO frequency and its second harmonic in GX 339-4 BHC evolves with this frequency. It is also was shown by different authors (see, e.g., Pahari et al. 2013; Zhang et al. 2017) that some distinct features are usually present in phase lag spectra on the QPO and its harmonics frequencies, if it is present.

First example of $\Delta\tau \propto f^{-0.7}$ behavior was found by Miyamoto and Kitamoto (1989) in Cyg X-1 and later investigated with much better resolution with just launched RXTE observatory by Nowak et al. (1999a). Miyamoto and Kitamoto (1989) tried to

explain observed lags with, dominant in that time, clumpy flow model, which previously was used to explain observed shape of the flat-top noise Fourier spectrum. Nowak et al. (1999b) considered two models, promising to explain observed hard lags and its dependence on frequency - i.e. phase lags are formed due to Comptonization in the extended corona or they formed due to the propagation of the perturbations in the advection flow. They found that it is hard to explain observed phase lags with both models, with first demanding very extended corona ($\sim 150R_g$ and second - very slow matter propagation speed in it. Later Kotov et al. (2001) considered their result and, on the basis on the amplitude and energy dependence of the hard lag, derived that it can not be caused by reverberation and is most preferably due to the perturbation propagation in the corona on the viscous time scales (see also Arévalo and Uttley 2006, on simulations results). It is worth mentioning, that proposed models are generally can explain hard lags but fail in explaining soft lags, which were later found in many source both on low and high frequencies (below and above flat-top noise break frequency) to mention a few (Gandhi et al. 2010; Cassatella et al. 2012; Yan et al. 2017; van den Eijnden et al. 2017). However, it was demonstrated that soft lags are possible in the propagation fluctuation model if outward movement of the disk surface density perturbations due to viscous evolution are also considered (Mushtukov et al. 2017). Reig et al. (2018) found that mean time lag strongly correlates with photon index of power law continuum, with time lag increasing with decreasing hardness. They proposed, that observed behavior can be explained with the Comptonization of soft photons by energetic electrons in a jet. van den Eijnden et al. (2017) found that the sign and amplitude of the phase lag at the QPO frequency depends on a system inclination.

Considering phase lags obtained in this work, in the frequency range, where phase lags are positive they can be described with $\Delta\phi/f \propto f^{-0.7}$ relation, which breaks at ~ 0.1 Hz, below which lags are negative. Unfortunately, due to insufficient signal to noise ratio, we can not determine, are any specific feature present at QPO or its second harmonic centroid frequency. Obtained phase lag dependence can be considered as quite standard for BHC.

5.4 *Swift-XRT* observations

We performed search for LF QPOs in first dozen of *Swift-XRT* observations of the GRS 1739–278. QPO is clearly detected in observations 3 to 9, with frequency varying from 0.37 Hz (during simultaneous observation with *NuSTAR*, see Fig. 2) up to 5.1 Hz (see Tab. 3). Last detection of QPO happened right before the onset of a strong flaring, at $\tau_0 + 46.6$.

We used the shape of power spectra in order to classify QPOs as belonging to type C or B (Casella et al. 2005). In all observations except for the observation 03, low frequency parts of power spectra can be described with weak red noise,

which typically accompanies type-B QPOs. In order to reinforce classification we calculated *rms* for each detected QPO, along with total *rms* over 0.01–20 Hz band. Obtained *rms_{total}* are significantly lower for observations 04..09 than for 03. We, therefore, conclude that in observations 04..09 type-B QPOs were observed with frequencies ranging from ~ 2 Hz to 5 Hz. It follows, that four days after the *NuSTAR* observation, the source already had transitioned from HIMS to SIMS and resided in this state until 09 *Swift-XRT* observation.

6 DISCUSSION AND CONCLUSIONS

We had studied *NuSTAR* observation carried out during the transition between soft and hard state. We had studied the spectro-timing evolution of GRS 1739–278 during its hard-intermediate state. We found a prominent type-C LF QPO in its power spectrum, its frequency show clear correlation with parameters of continuum emission. As the QPO frequency increases from 0.3 to 0.7 Hz spectrum became softer: the power law index grows from 1.46 to 1.53 and cut-off energy decreases from 30 to 26 keV. Overall flux increases, too. Such behaviour was first observed in a number of systems by Di Matteo and Psaltis (1999) and now it is studied in greater details in many systems (see e.g. Vignarca et al. 2003; Stiele et al. 2013; Seifina et al. 2014; Fürst et al. 2016, and many more). Although the quality of a data prevented us from measuring a movement of the inner disk boundary, from the total broadband spectrum we found that an accretion disk is truncated at radius smaller than $9 GM/c^2$ (90% confidence limit) which is in agreement with an estimates by Miller et al. (2015). We used this combination of inner radius and QPO together with Lense-Thirring precession model of QPO origin (Ingram et al. 2009) in order to assess black hole mass. Following Ingram and Motta (2014) we calculated nodal frequencies (which is thought to correspond to QPO fundamental frequency) versus inner radius for two values of the black hole mass ($10M_\odot$ and $30M_\odot$) and two values of spin - $a = 0.1$ and $a = 0.998$ (maximally rotating). As it can be seen from Fig. 11 observations are incompatible with black hole mass $10M_\odot$ and barely agrees with slowly rotating massive black hole. This results, along with measurements by Fürst et al. (2016), indicate that there are some tensions between predictions of RPM and truncation radii inferred from spectral fitting.

We carried out extensive study of timing properties of the GRS 1739–278. Along with the broadband noise and fundamental QPO, second harmonic of QPO is clearly seen. During several intervals from first half of the observation subharmonic is also observed. In all 13 intervals second QPO harmonic is more prominent in soft band (3–5 keV), with ratio of its amplitude to that of fundamental QPO being 0.565 ± 0.02 in 3–5 keV band versus 0.275 ± 0.02 in 15–78 keV. We also measured velocity of the QPO drift and found it to be $\approx 6.0 \times 10^{-6}$ Hz s $^{-1}$.

We searched for similar QPO in *Swift-XRT* observations of GRS 1739–278 performed after *NuSTAR* exposure and found that all other detected QPOs are probably of type B, thus that the source transitioned to soft-intermediate state few days after *NuSTAR* observation.

Coherence measured between adjacent energy ranges in

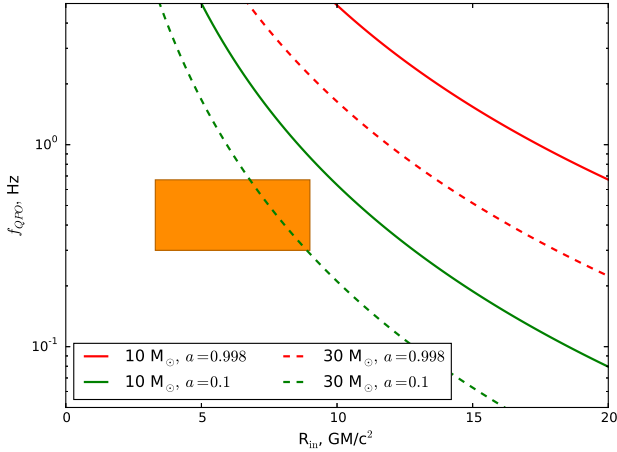


Figure 11. Expected QPO frequency for a black hole of a given mass and spin versus inner disk radius from Ingram and Motta (2014). Orange square represent region containing observed QPOs.

0.01–1 Hz was found to be nearly unity, while for distant energy bands coherence turned out to be lower. In the frame of the propagating fluctuations model it can indicate on the presence of partially independent radial flows.

Phase lag found to be of order of +0.1 s (hard) in the 0.1–3 Hz frequency range and $-1..-0.1$ s (soft) below 0.1 Hz. van den Eijnden et al. (2017) shown that the sign of the phase lag on the type-C QPO centroid frequency depends on a system inclination, however this difference is explicit only when QPO centroid frequency is above ~ 3 Hz.

ACKNOWLEDGMENTS

The work was supported by the Russian Science Foundation (grant no. 14-12-01287). We thank E.M. Churazov for fruitful discussions and important suggestions. We are grateful for T.Dauser and J.Gracia for their help with *relxill* model. This research has made use of data obtained through the High Energy Astrophysics Science Archive Research Center Online Service, provided by the NASA/Goddard Space Flight Center. This work made use of data supplied by the UK Swift Science Data Centre at the University of Leicester.

REFERENCES

Allen, C. W.: 1973, *Astrophysical quantities*
 Arévalo, P. and Uttley, P.: 2006, *MNRAS* **367**, 801
 Arnaud, K. A.: 1996, in G. H. Jacoby and J. Barnes (eds.), *Astronomical Data Analysis Software and Systems V*, Vol. 101 of *Astronomical Society of the Pacific Conference Series*, p. 17
 Bachetti, M., Harrison, F. A., Cook, R., Tomsick, J., Schmid, C., Grefenstette, B. W., Barret, D., Boggs, S. E., Christensen, F. E., Craig, W. W., Fabian, A. C., Fürst, F., Gandhi, P., Hailey, C. J., Kara, E., Maccarone, T. J., Miller, J. M., Pottschmidt, K., Stern, D., Uttley, P., Walton, D. J., Wilms, J., and Zhang, W. W.: 2015, *ApJ* **800**, 109
 Belloni, T. and Hasinger, G.: 1990, *A&A* **227**, L33

Belloni, T. M.: 2010, in T. Belloni (ed.), *Lecture Notes in Physics*, Berlin Springer Verlag, Vol. 794 of *Lecture Notes in Physics*, Berlin Springer Verlag, p. 53
 Böck, M., Grinberg, V., Pottschmidt, K., Hanke, M., Nowak, M. A., Markoff, S. B., Uttley, P., Rodriguez, J., Pooley, G. G., Suchy, S., Rothschild, R. E., and Wilms, J.: 2011, *A&A* **533**, A8
 Borozdin, K. N., Revnivtsev, M. G., Trudolyubov, S. P., Aleksandrovich, N. L., Sunyaev, R. A., and Skinner, G. K.: 1998, *Astronomy Letters* **24**, 435
 Borozdin, K. N. and Trudolyubov, S. P.: 2000, *ApJ* **533**, L131
 Cabanac, C., Henri, G., Petrucci, P.-O., Malzac, J., Ferreira, J., and Belloni, T. M.: 2010, *MNRAS* **404**, 738
 Casella, P., Belloni, T., and Stella, L.: 2005, *ApJ* **629**, 403
 Cassatella, P., Uttley, P., and Maccarone, T. J.: 2012, *MNRAS* **427**, 2985
 Churazov, E., Gilfanov, M., and Revnivtsev, M.: 2001, *MNRAS* **321**, 759
 Dauser, T., García, J., Parker, M. L., Fabian, A. C., and Wilms, J.: 2014, *MNRAS* **444**, L100
 Dauser, T., García, J., Walton, D. J., Eikmann, W., Kallman, T., McClintock, J., and Wilms, J.: 2016, *A&A* **590**, A76
 De Marco, B., Ponti, G., Petrucci, P. O., Clavel, M., Corbel, S., Belmont, R., Chakravorty, S., Coriat, M., Drappeau, S., Ferreira, J., Henri, G., Malzac, J., Rodriguez, J., Tomsick, J. A., Ursini, F., and Zdziarski, A. A.: 2017, *MNRAS* **471**, 1475
 Di Matteo, T. and Psaltis, D.: 1999, *ApJ* **526**, L101
 Dickey, J. M. and Lockman, F. J.: 1990, *ARA&A* **28**, 215
 Eardley, D. M., Lightman, A. P., and Shapiro, S. L.: 1975, *ApJ* **199**, L153
 Evans, P. A., Beardmore, A. P., Page, K. L., Osborne, J. P., O’Brien, P. T., Willingale, R., Starling, R. L. C., Burrows, D. N., Godet, O., Vetere, L., Racusin, J., Goad, M. R., Wiersema, K., Angelini, L., Capaldi, M., Chincarini, G., Gehrels, N., Kennea, J. A., Margutti, R., Morris, D. C., Mountford, C. J., Pagani, C., Perri, M., Romano, P., and Tanvir, N.: 2009, *MNRAS* **397**, 1177
 Filippova, E., Kuulkers, E., Skådt, N. M., Alfonso-Garzon, J., Beckmann, V., Bird, A. J., Brandt, S., Chenevez, J., Del Santo, M., Domingo, A., Ebisawa, K., Jonker, P. G., Kretschmar, P., Markwardt, C. B., Oosterbroek, T., Paizis, A., Pottschmidt, K., Sanchez-Fernandez, C., Wijnands, R., Bozzo, E., and Ferrigno, C.: 2014, *The Astronomer’s Telegram* 5991
 Fuerst, F., Tomsick, J. A., Yamaoka, K., Dauser, T., Miller, J. M., Clavel, M., Corbel, S., Fabian, A. C., Garcia, J., Harrison, F. A., Loh, A., Kaaret, P., Kalemci, E., Migliari, S., Miller-Jones, J. C. A., Pottschmidt, K., Rahoui, F., Rodriguez, J., Stern, D., Stuhlinger, M., Walton, D. J., and Wilms, J.: 2016, *ArXiv e-prints*
 Fürst, F., Grinberg, V., Tomsick, J. A., Bachetti, M., Boggs, S. E., Brightman, M., Christensen, F. E., Craig, W. W., Gandhi, P., Grefenstette, B., Hailey, C. J., Harrison, F. A., Madsen, K. K., Parker, M. L., Pottschmidt, K., Stern, D., Walton, D. J., Wilms, J., and Zhang, W. W.: 2016, *ApJ* **828**, 34
 Gandhi, P., Dhillon, V. S., Durant, M., Fabian, A. C., Kubota, A., Makishima, K., Malzac, J., Marsh, T. R., Miller, J. M., Shahbaz, T., Spruit, H. C., and Casella, P.: 2010, *MNRAS* **407**, 2166
 García, J., Dauser, T., Reynolds, C. S., Kallman, T. R., McClintock, J. E., Wilms, J., and Eikmann, W.: 2013, *ApJ* **768**, 146
 Gierliński, M., Middleton, M., Ward, M., and Done, C.: 2008, *Nature* **455**, 369
 Grebenev, S. A., Sunyaev, R. A., and Pavlinsky, M. N.: 1997, *Advances in Space Research* **19**, 15
 Greiner, J., Dennerl, K., and Predehl, P.: 1996, *A&A* **314**, L21
 Harrison, F. A., Craig, W. W., Christensen, F. E., Hailey, C. J.,

- Zhang, W. W., Boggs, S. E., Stern, D., Cook, W. R., Forster, K., Giommi, P., Grefenstette, B. W., Kim, Y., Kitaguchi, T., Koglin, J. E., Madsen, K. K., Mao, P. H., Miyasaka, H., Mori, K., Perri, M., Pivovarov, M. J., Puccetti, S., Rana, V. R., Westergaard, N. J., Willis, J., Zoglauer, A., An, H., Bachetti, M., Barrière, N. M., Bellm, E. C., Bhalerao, V., Brejnholt, N. F., Fuerst, F., Liebe, C. C., Markwardt, C. B., Nynka, M., Vogel, J. K., Walton, D. J., Wik, D. R., Alexander, D. M., Cominsky, L. R., Hornschemeier, A. E., Hornstrup, A., Kaspi, V. M., Madejski, G. M., Matt, G., Molendi, S., Smith, D. M., Tomsick, J. A., Ajello, M., Ballantyne, D. R., Baloković, M., Barret, D., Bauer, F. E., Blandford, R. D., Brandt, W. N., Brenneman, L. W., Chiang, J., Chakrabarty, D., Chenevez, J., Comastri, A., Dufour, F., Elvis, M., Fabian, A. C., Farrah, D., Fryer, C. L., Gotthelf, E. V., Grindlay, J. E., Helfand, D. J., Krivonos, R., Meier, D. L., Miller, J. M., Natalucci, L., Ogle, P., Ofek, E. O., Ptak, A., Reynolds, S. P., Rigby, J. R., Tagliaferri, G., Thorsett, S. E., Treister, E., and Urry, C. M.: 2013, *ApJ* **770**, 103
- Heil, L. M., Uttley, P., and Klein-Wolt, M.: 2015, *MNRAS* **448**, 3339
- Hjellming, R. M., Rupen, M. P., Marti, J., Mirabel, F., and Rodriguez, L. F.: 1996, *IAU Circ.* 6383
- Homan, J. and Belloni, T.: 2005, *Ap&SS* **300**, 107
- Homan, J., Wijnands, R., van der Klis, M., Belloni, T., van Paradijs, J., Klein-Wolt, M., Fender, R., and Méndez, M.: 2001, *ApJS* **132**, 377
- Huppenkothen, D. and Bachetti, M.: 2017, *ArXiv e-prints*
- Ingram, A., Done, C., and Fragile, P. C.: 2009, *MNRAS* **397**, L101
- Ingram, A. and Motta, S.: 2014, *MNRAS* **444**, 2065
- Ingram, A. and van der Klis, M.: 2013, *MNRAS* **434**, 1476
- Ingram, A. and van der Klis, M.: 2015, *MNRAS* **446**, 3516
- Ingram, A., van der Klis, M., Middleton, M., Done, C., Altamirano, D., Heil, L., Uttley, P., and Axelsson, M.: 2016, *MNRAS* **461**, 1967
- James, F. and Roos, M.: 1975, *Comput. Phys. Commun.* **10**, 343
- Ji, J. F., Zhang, S. N., Qu, J. L., and Li, T. P.: 2003, *ApJ* **584**, L23
- Kalberla, P. M. W., Burton, W. B., Hartmann, D., Arnal, E. M., Bajaja, E., Morras, R., and Pöppel, W. G. L.: 2005, *A&A* **440**, 775
- Kotov, O., Churazov, E., and Gilfanov, M.: 2001, *MNRAS* **327**, 799
- Krimm, H. A., Barthelmy, S. D., Baumgartner, W., Cummings, J., Gehrels, N., Lien, A. Y., Markwardt, C. B., Palmer, D., Sakamoto, T., Stamatikos, M., and Ukwatta, T.: 2014, *The Astronomer's Telegram* 5986
- Krimm, H. A., Holland, S. T., Corbet, R. H. D., Pearlman, A. B., Romano, P., Kennea, J. A., Bloom, J. S., Barthelmy, S. D., Baumgartner, W. H., Cummings, J. R., Gehrels, N., Lien, A. Y., Markwardt, C. B., Palmer, D. M., Sakamoto, T., Stamatikos, M., and Ukwatta, T. N.: 2013, *ApJS* **209**, 14
- Lyubarskii, Y. E.: 1997, *MNRAS* **292**, 679
- Malzac, J., Belloni, T., Spruit, H. C., and Kanbach, G.: 2003, *A&A* **407**, 335
- Marshall, D. J., Robin, A. C., Reylé, C., Schultheis, M., and Picaud, S.: 2006, *A&A* **453**, 635
- Marti, J., Mirabel, I. F., Duc, P.-A., and Rodriguez, L. F.: 1997, *A&A* **323**, 158
- Matsuoka, M., Kawasaki, K., Ueno, S., Tomida, H., Kohama, M., Suzuki, M., Adachi, Y., Ishikawa, M., Mihara, T., Sugizaki, M., Isobe, N., Nakagawa, Y., Tsunemi, H., Miyata, E., Kawai, N., Kataoka, J., Morii, M., Yoshida, A., Negoro, H., Nakajima, M., Ueda, Y., Chujo, H., Yamaoka, K., Yamazaki, O., Nakahira, S., You, T., Ishiwata, R., Miyoshi, S., Eguchi, S., Hiroi, K., Katayama, H., and Ebisawa, K.: 2009, *PASJ* **61**, 999
- Mauche, C. W.: 2002, *ApJ* **580**, 423
- Méndez, M., Altamirano, D., Belloni, T., and Sanna, A.: 2013, *MNRAS* **435**, 2132
- Mereminskiy, I. A., Filippova, E. V., Krivonos, R. A., Grebenev, S. A., Burenin, R. A., and Sunyaev, R. A.: 2017, *Astronomy Letters* **43**, 167
- Miller, J. M., Homan, J., and Miniutti, G.: 2006a, *ApJ* **652**, L113
- Miller, J. M., Homan, J., Steeghs, D., Rupen, M., Hunstead, R. W., Wijnands, R., Charles, P. A., and Fabian, A. C.: 2006b, *ApJ* **653**, 525
- Miller, J. M., Tomsick, J. A., Bachetti, M., Wilkins, D., Boggs, S. E., Christensen, F. E., Craig, W. W., Fabian, A. C., Grefenstette, B. W., Hailey, C. J., Harrison, F. A., Kara, E., King, A. L., Stern, D. K., and Zhang, W. W.: 2015, *ApJ* **799**, L6
- Miyamoto, S. and Kitamoto, S.: 1989, *Nature* **342**, 773
- Miyamoto, S., Kitamoto, S., Iga, S., Negoro, H., and Terada, K.: 1992, *ApJ* **391**, L21
- Molteni, D., Sponholz, H., and Chakrabarti, S. K.: 1996, *ApJ* **457**, 805
- Muñoz-Darias, T., Motta, S., Stiele, H., and Belloni, T. M.: 2011, *MNRAS* **415**, 292
- Mushtukov, A. A., Ingram, A., and van der Klis, M.: 2017, *ArXiv e-prints*
- Narayan, R. and Yi, I.: 1995, *ApJ* **452**, 710
- Nowak, M. A., Wilms, J., and Dove, J. B.: 1999a, *ApJ* **517**, 355
- Nowak, M. A., Wilms, J., Vaughan, B. A., Dove, J. B., and Begelman, M. C.: 1999b, *ApJ* **515**, 726
- Pahari, M., Neilsen, J., Yadav, J. S., Misra, R., and Uttley, P.: 2013, *ApJ* **778**, 136
- Parker, M. L., Tomsick, J. A., Miller, J. M., Yamaoka, K., Lohfink, A., Nowak, M., Fabian, A. C., Alston, W. N., Boggs, S. E., Christensen, F. E., Craig, W. W., Fürst, F., Gandhi, P., Grefenstette, B. W., Grinberg, V., Hailey, C. J., Harrison, F. A., Kara, E., King, A. L., Stern, D., Walton, D. J., Wilms, J., and Zhang, W. W.: 2015, *ApJ* **808**, 9
- Paul, J., Bouchet, L., Churazov, E., and Sunyaev, R.: 1996, *IAU Circ.* 6348
- Paul, J., Mandrou, P., Ballet, J., Cantin, M., Chabaud, J., Cordier, B., Ehanno, M., Goldwurm, A., Lambert, A., Lande, J., et al.: 1991, *Advances in Space Research* **11**(8), 289
- Pottschmidt, K., Wilms, J., Nowak, M. A., Pooley, G. G., Gleissner, T., Heindl, W. A., Smith, D. M., Remillard, R., and Staubert, R.: 2003, *A&A* **407**, 1039
- Reig, P., Kylafis, N. D., Papadakis, I. E., and Costado, M. T.: 2018, *MNRAS* **473**, 4644
- Reig, P., Martínez-Núñez, S., and Reglero, V.: 2006, *A&A* **449**, 703
- Remillard, R. A. and McClintock, J. E.: 2006, *ARA&A* **44**, 49
- Revnivtsev, M., Gilfanov, M., and Churazov, E.: 2000, *A&A* **363**, 1013
- Ross, R. R. and Fabian, A. C.: 2005, *MNRAS* **358**, 211
- Schultheis, M., Chen, B. Q., Jiang, B. W., Gonzalez, O. A., Enokiya, R., Fukui, Y., Torii, K., Rejkuba, M., and Minniti, D.: 2014, *A&A* **566**, A120
- Seifina, E., Titarchuk, L., and Shaposhnikov, N.: 2014, *ApJ* **789**, 57
- Shakura, N. I. and Sunyaev, R. A.: 1973, *A&A* **24**, 337
- Shapiro, S. L., Lightman, A. P., and Eardley, D. M.: 1976, *ApJ* **204**, 187
- Stella, L. and Vietri, M.: 1998, *ApJ* **492**, L59
- Stiele, H., Belloni, T. M., Kalemci, E., and Motta, S.: 2013, *MNRAS* **429**, 2655
- Tagger, M. and Pellat, R.: 1999, *A&A* **349**, 1003
- Tanaka, Y. and Shibasaki, N.: 1996, *ARA&A* **34**, 607
- Terrell, Jr., N. J.: 1972, *ApJ* **174**, L35
- García, J., Dauser, T., Lohfink, A., Kallman, T. R., Steiner, J. F., McClintock, J. E., Brenneman, L., Wilms, J., Eikmann, W., Reynolds, C. S., and Tombesi, F.: 2014, *ApJ* **782**, 76

- Uttley, P., Cackett, E. M., Fabian, A. C., Kara, E., and Wilkins, D. R.: 2014, *A&ARv* **22**, 72
- van den Eijnden, J., Ingram, A., Uttley, P., Motta, S. E., Belloni, T. M., and Gardenier, D. W.: 2017, *MNRAS* **464**, 2643
- Vaughan, B. A. and Nowak, M. A.: 1997, *ApJ* **474**, L43
- Verner, D. A., Ferland, G. J., Korista, K. T., and Yakovlev, D. G.: 1996, *ApJ* **465**, 487
- Vignarca, F., Migliari, S., Belloni, T., Psaltis, D., and van der Klis, M.: 2003, *A&A* **397**, 729
- Vikhlinin, A., Churazov, E., and Gilfanov, M.: 1994, *A&A* **287**, 73
- Wijnands, R., Méndez, M., Miller, J. M., and Homan, J.: 2001, *MNRAS* **328**, 451
- Wijnands, R. and van der Klis, M.: 1999, *ApJ* **514**, 939
- Wilms, J., Allen, A., and McCray, R.: 2000, *ApJ* **542**, 914
- Yan, S.-P., Ji, L., Méndez, M., Liu, S.-M., Wang, N., Li, X.-D., Ge, M.-Y., Liao, J.-Y., Niu, S., Qu, J.-L., Ding, G.-Q., Liu, Q.-Z., and Sun, W.: 2017, *MNRAS* **465**, 1926
- Yan, Z. and Yu, W.: 2017, *Monthly Notices of the Royal Astronomical Society* **470**(4), 4298
- Zhang, L., Wang, Y., Méndez, M., Chen, L., Qu, J., Altamirano, D., and Belloni, T.: 2017, *ApJ* **845**, 143
- Zhang, W., Jahoda, K., Swank, J. H., Morgan, E. H., and Giles, A. B.: 1995, *ApJ* **449**, 930

This paper has been typeset from a \LaTeX file prepared by the author.